Article

Microstructure and First Hydrogenation Properties of Ti$_{30}$V$_{60}$Mn$_{(10-x)}$Cr$_x$ (x = 0, 3.3, 6.6, 10) + 4 wt.% Zr

Chourouk Kefi and Jacques Huot *

Hydrogen Research Institute, Université du Québec à Trois-Rivières, 3351 des Forges, Trois-Rivières, QC G9A 5H7, Canada; chourouk.kefi@uqtr.ca
* Correspondence: jacques.huot@uqtr.ca

Abstract: In this paper, we studied the effect of the Cr/Mn ratio on the microstructure, crystal structure and hydrogen absorption properties of the quaternary alloys of compositions Ti$_{30}$V$_{60}$Mn$_{(10-x)}$Cr$_x$ (x = 0, 3.3, 6.6 and 10) + 4 wt.% Zr. The addition of Hf instead of Zr was also investigated. We found that all alloys are single-phase BCC (Body Centred Cubic) but with regions of high concentration of Zr (or Hf). The first hydrogenation at room temperature under 2 MPa of hydrogen happens quickly without any incubation time. The Ti$_{30}$V$_{60}$Mn$_{3.3}$Cr$_{6.6}$ + 4 wt.% Zr alloy showed the fastest kinetics and highest hydrogen absorption (3.8 wt.%). For this composition, replacing Zr with Hf made the first hydrogenation slower and reduced the capacity to 3.4 wt.%. No activation was observed for the same alloy without additives. As the alloy without additives did not absorb hydrogen at all, it means that the presence of these high concentrations of Zr (or Hf) is essential for quick first hydrogenation.

Keywords: hydrogen storage; metal hydride; first hydrogenation; BCC alloys

1. Introduction

For hydrogen storage applications, metal hydrides have the benefit of storing hydrogen with high volumetric storage density, low cost [1] and safety [2]. Several types of intermetallic compounds have been investigated for hydrogen storage: AB$_2$ [3], AB$_5$ [4], LaNi$_5$ [5,6] TiFe [7,8], and ZrV$_2$ [9]. Mg-based alloys have a large capacity, but their temperature of operation is usually too high for most practical applications [10–13]. Solid solution alloys such as Ti–V-based Body Centred Cubic (BCC) alloys have a hydrogen-to-metal ratio (H/M) of about 2 at low pressure and room temperature [14–17]. However, poor activation (first hydrogenation) at ambient conditions increases the cost of these metal hydrides for commercial applications. Several approaches have been attempted to enhance the activation such as microstructural refinement [18,19] or adding other elements such as Zr [20,21]. The substitution of a small amount of transition elements such as Fe, Co, Ni, Mn or Cr could be beneficial for the first hydrogenation but usually changes the hydrogenation thermodynamics [22–26]. One BCC Ti–V–M system that has been intensively studied is Ti–V–Mn [27–31]. For example, a small change in composition in Ti$_{0.5}$V$_{0.5\pm x}$Mn (x = −0.04 and 0.01) alloy results in a significant change in plateau pressure and hysteresis [28].

According to many investigations, introducing a secondary C14 Laves phase into the BCC solid solution by adding alloying elements promotes hydrogen diffusion and its absorption in the material [28,32–36]. Substitution may lead to an easy activation of the alloys, but the hydrogen storage capacity could be reduced. For instance, it has been reported that increasing the Zr content in Ti$_{10}$V$_{(84-x)}$Fe$_6$Zr$_x$ (x = 1, 2, 4, 6, 8) alloys leads to an increase in the ratio of C14/BCC which results in a better activation behaviour although it decreases the hydrogen capacity [37]. Mouri and Iba investigated the hydrogen storage properties of Ti$_1$V$_x$Mn$_{2-x}$ (x = 1.4–0.6) and found that the fresh surfaces formed in Laves phases promote the activation, and that increasing the Mn content leads to the total elimination of the BCC phase and the reduction of the capacity of the alloy [38].

Miraglia et al., have shown that in the Ti–V–Cr BCC alloy, adding 4 wt.% of Zr_7Ni_{10} could improve the activation process under mild temperature and hydrogen pressure [39]. More recently, it was reported that by adding only 4 wt.% of Zr to Ti–V–Cr BCC alloy, a Zr-rich secondary phase was found in the as-cast alloy [40,41]. This phase is probably responsible for the fast activation kinetics and the high hydrogen capacity.

One of the aims of the current work is to improve the properties of Ti–V–Mn in terms of activation and hydrogen capacity by substituting Mn with the transition metal Cr. In this paper, we present the microstructure, crystal structure and hydrogenation properties of $Ti_{30}V_{60}Mn_{(10-x)}Cr_x$ ($x = 0$, 3.3, 6.6 and 10) alloy added with 4 wt.% of Zr. Such a small amount of Zr was added in order not to drastically change the crystal structure and hydrogen capacity of the alloy. The effect of using Hf instead of Zr as an additive was also investigated. This was justified because Hf is a common impurity in Zr. In addition, as the atomic radius of Hf and Zr are practically identical, this enables us to distinguish the effect of atomic radius and the element chemistry.

2. Materials and Methods

2.1. Alloy Synthesis

Alloys with nominal composition $Ti_{30}V_{60}Mn_{(10-x)}Cr_x$ ($x = 0$, 3.3, 6.6 and 10) + 4 wt.% Zr were prepared by arc melting under an argon atmosphere. The raw materials vanadium (irregular pieces, 99.7%), titanium (sponge, 3–19 mm, 99.95%), manganese (irregular pieces, 99.5%), chromium (irregular pieces, 99.0%) and zirconium (sponge 0.8–25.4 mm, 99.95%) were purchased from Alfa Aesar (Ward Hill, MA, USA) and used as received. Each ingot ($\approx$3 g) was turned over and remelted three times to ensure good homogeneity. To compensate for the loss of the manganese during arc melting due to its boiling point (2061 °C) which is close to the melting point of the other elements, an excess of 20 wt.% was added to the nominal abundance of manganese. The alloy $Ti_{30}V_{60}Mn_{3.3}Cr_{6.6}$ + 8 wt.%Hf was cast, using hafnium (irregular pieces 99.7%) from Alfa Aesar (Ward Hill, MA, USA). The as-cast alloys in button shape were hand-crushed in an argon-filled glovebox using a hardened steel mortar and pestle.

2.2. Crystal Structure and Morphology

The phase composition and crystal structure of the alloys were investigated by X-ray diffraction (XRD) using a Bruker D8 Focus powder diffractometer (Madison, WI, USA) with Cu Kα radiation. The XRD patterns were analyzed by the Rietveld method using Topas V6 software [42]. The microstructure of each sample was observed using a Hitachi SU1510 scanning electron microscope (SEM) (Hitachi High-Tech Canada, Toronto, Ontario, Canada) in the backscattered electron mode (BSE). The chemical composition was measured by Energy Dispersive X-ray Spectroscopy (EDX) using Oxford Instrument X-Max (Abingdon, UK) analytical resolution.

2.3. Hydrogen Absorption and Desorption Measurements

First hydrogenation tests were performed by using a homemade Sievert apparatus. In this type of apparatus, the quantity of hydrogen absorbed or desorbed is measured by the pressure change in a calibrated volume during the reaction. Crushed samples weighing around 1 g were placed in a sample holder and evacuated for 15 min at room temperature prior to kinetic measurement under 2 MPa of hydrogen at room temperature (25 °C). This mode was chosen because one of the goals of this investigation was to find alloys that could be easily hydrogenated under mild conditions.

3. Results

3.1. Morphologie

The backscattered electron SEM images of the as-cast alloys are shown in Figure 1. For the composition $Ti_{30}V_{60}Mn_{3.3}Cr_{6.6}$ cast without zirconium shown in Figure 1a, the alloy is basically a single phase. With the addition of 4 wt.% Zr, all alloys show a microstructure

consisting of a grey matrix and bright regions. For the $Ti_{30}V_{60}Mn_{10}$ alloy, black regions are also present. It is noticeable that, with an increasing amount of chromium, the number of bright regions is also increasing. The dark spots in Figure 1a,c–e are holes formed during the synthesis process.
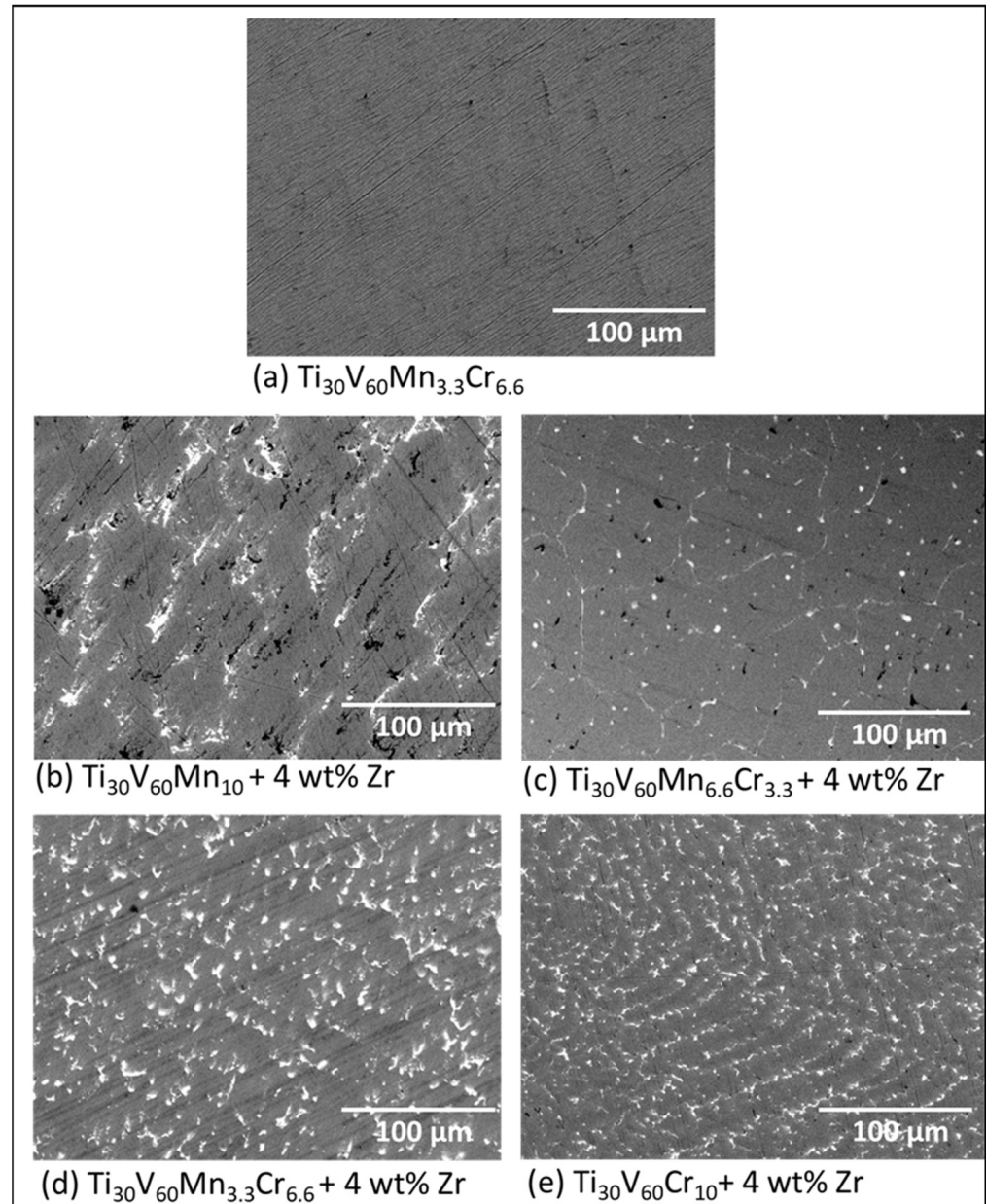

Figure 1. Backscattered electron images of (**a**) $Ti_{30}V_{60}Mn_{3.3}Cr_{6.6}$ and $Ti_{30}V_{60}Mn_{(10-x)}Cr_x$ + 4 wt.% Zr with (**b**) $x = 0$, (**c**) $x = 3.3$, (**d**) $x = 6.6$, (**e**) $x = 10$.

Elemental mapping and area analysis were performed on the alloys to determine the distribution of the elements. The quantitative assessment of the chemical composition of the bulk and the individual phases was performed by EDX measurements and the results are shown in Table 1.

Table 1. Elemental abundance of the alloys for bulk and individual region compositions as measured from EDX. Error on the last significant digit is indicated in parentheses.

Sample	Region	Ti (at.%)	V (at.%)	Mn (at.%)	Cr (at.%)	Zr (at.%)
$Ti_{30}V_{60}Mn_{10}$ + 4 wt.% Zr	nominal	30.9	58.2	8.9	-	2
	Bulk measured	32.2(1)	57.9(1)	6.3(1)	-	3.7(1)
$Ti_{30}V_{60}Mn_{10}$ + 4 wt.% Zr	Matrix	31.2(8)	60(1)	6.5(3)	-	2.3(3)
	Bright region	41.4(1)	28(1)	3.6(1)	-	27(1)
	Black region	78.7(1)	10.7(8)	0.7(1)	-	9.9(5)
$Ti_{30}V_{60}Mn_{6.6}Cr_{3.3}$ + 4 wt.% Zr	nominal	30.8	58.1	6	3.1	2
	Bulk measured	30.4(1)	57.1(1)	6.2(1)	2.9(1)	3.4(1)
$Ti_{30}V_{60}Mn_{6.6}Cr_{3.3}$ + 4 wt.% Zr	Matrix	30.7(4)	57.5(4)	6(6)	2.90(4)	2.9(1)
	Bright region	38.7(1)	29.2(1)	3(1)	1.4(1)	27.7(1)
$Ti_{30}V_{60}Mn_{3.3}Cr_{6.6}$ + 4 wt.% Zr	nominal	30.8	58	2.9	6.3	1.9
	Bulk measured	28.7(1)	58.5(1)	3.6(1)	6.2(1)	3.3(1)
$Ti_{30}V_{60}Mn_{3.3}Cr_{6.6}$ + 4 wt.% Zr	Matrix	27.8(8)	62(1)	3.2(1)	6.10(5)	1.1(2)
	Bright region	39.9(5)	26(1)	2.7(1)	3.0(2)	28(1)
$Ti_{30}V_{60}Cr_{10}$ + 4 wt.% Zr	nominal	30.7	58	-	9.5	1.9
	Bulk measured	29.6(1)	57.7(1)	-	9.9(1)	2.8(1)
$Ti_{30}V_{60}Cr_{10}$ + 4 wt.% Zr	Matrix	29.2(9)	59(1)	-	9.8(2)	2(5)
	Bright region	41.6(4)	29.5(2)	-	4.9(2)	24(3)
$Ti_{30}V_{60}Mn_{3.3}Cr_{6.6}$ (Zr-free)	nominal	31.4	59.2	3	6.4	-
	Bulk measured	31.0(1)	59.1(1)	3.5(1)	6.4(1)	-
$Ti_{30}V_{60}Mn_{3.3}Cr_{6.6}$ (Zr-free)	Matrix	31.1(3)	59(3)	3.6(4)	6.3(1)	-

For $Ti_{30}V_{60}Mn_{10}$ + 4 wt.% Zr (Figure 2) the titanium, vanadium and manganese are homogeneously distributed throughout the matrix. The bright areas are rich in zirconium while the black regions are titanium-rich.
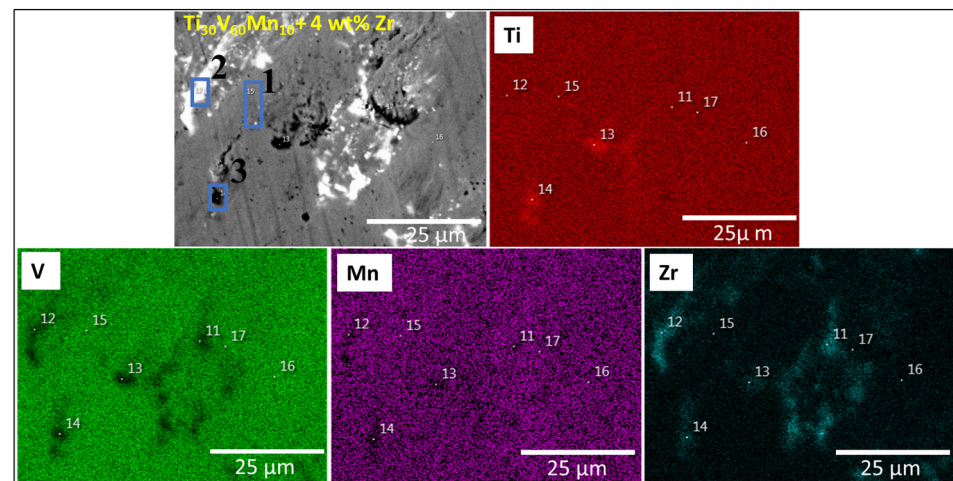

Figure 2. Backscattered electron micrograph of $Ti_{30}V_{60}Mn_{10}$ + 4 wt.% Zr alloy with EDX mappings and chemical compositions at different sites.

Figure 3 shows the $Ti_{30}V_{60}Mn_{6.6}Cr_{3.3}$ + 4wt.% Zr alloy. The matrix composition is very close to the nominal value. Zirconium is mainly in the bright region. There is no titanium-rich region. The dark spots are holes formed during casting.

The $Ti_{30}V_{60}Mn_{3.3}Cr_{6.6}$ + 4 wt.% Zr alloy shown in Figure 4 has a grey matrix with basically the nominal composition. The bright areas have a very high proportion of Zr.

The microstructure of $Ti_{30}V_{60}Cr_{10}$ + 4 wt.% Zr is presented in Figure 5. The matrix has a chemical composition close to the nominal value. The bright regions have a high proportion of Zr.
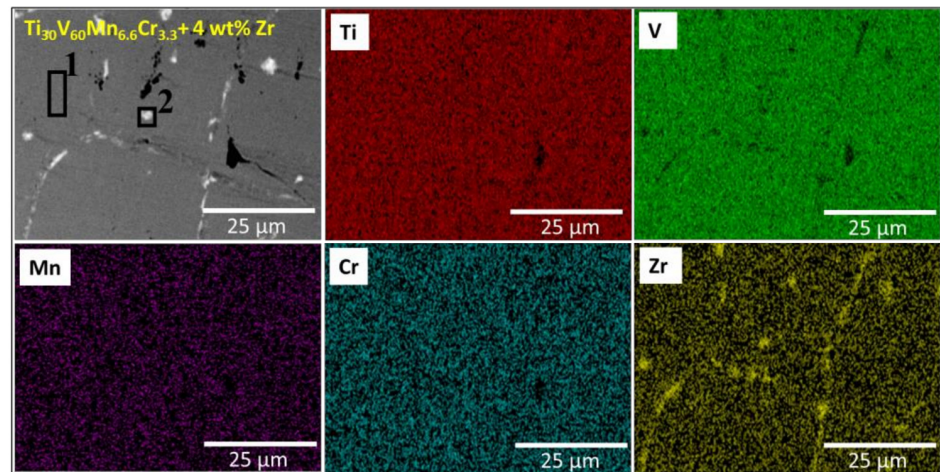
Figure 3. Backscattered electron micrograph of $Ti_{30}V_{60}Mn_{6.6}Cr_{3.3}+ 4$ wt.% Zr alloy with EDX mappings and chemical compositions at different sites.
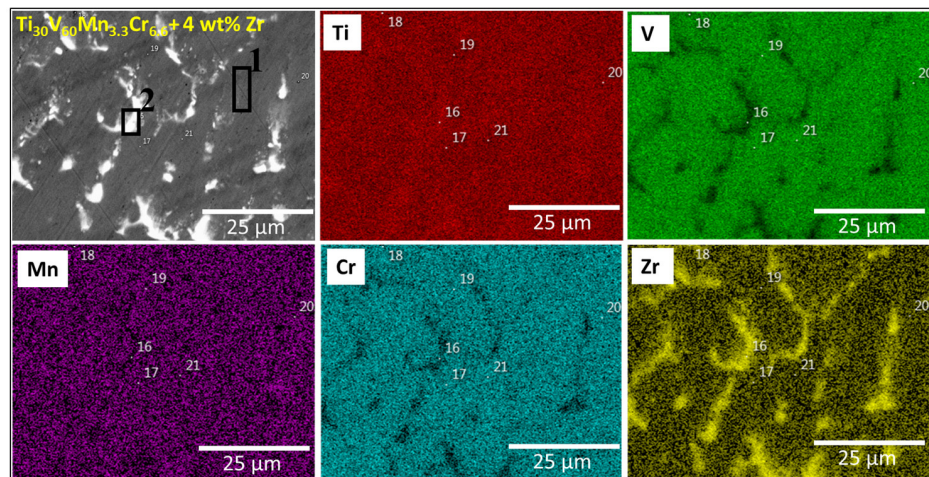
Figure 4. Backscattered electron micrograph of $Ti_{30}V_{60}Mn_{3.3}Cr_{6.6.}+ 4$ wt.% Zr alloy with EDX mappings and chemical compositions at different sites.
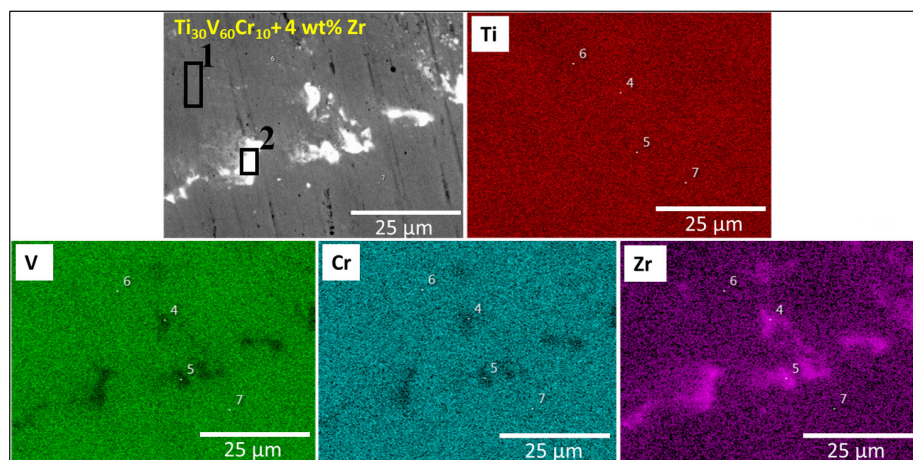
Figure 5. Backscattered electron micrograph of $Ti_{30}V_{60}Cr_{10.}+ 4$ wt.% Zr alloy with EDX mappings and chemical compositions at different sites.

For all the alloys, there was a good agreement between the bulk chemical compositions and the nominal values. As seen in Table 1, the bright regions of these alloys have similar

values. Compared to the matrix, in the bright areas, the proportion of Ti and Zr increases while the proportion of V, Mn and Cr decreases. In fact, a detailed inspection of these regions shows that they have a general composition close to $Ti_{\approx0.4}$ $V_{\approx0.3}(Mn+Cr)_{\approx0.05}$ $Zr_{\approx0.28}$.

To get a better view of the relationship between the matrix and the bright area, a line analysis was performed on the as-cast $Ti_{30}V_{60}Mn_{3.3}Cr_{6.6}$ + 4 wt.% Zr alloy. Figure 6 shows a continuous change in composition between the matrix and the bright area. The proportion of Ti and Zr increases in the brighter region while the proportion of V, Mn and Cr decreases. The biggest difference in proportion between the matrix and the bright region is for V and Zr. It is important to notice that there is no sharp boundary between the matrix and the bright area. We were not able to find a stable phase with similar composition in the literature. This may be an indication that this is a metastable phase. We are planning to synthesize an alloy with this nominal composition. This will give us some indication of the stability of this phase and also its crystal structure.
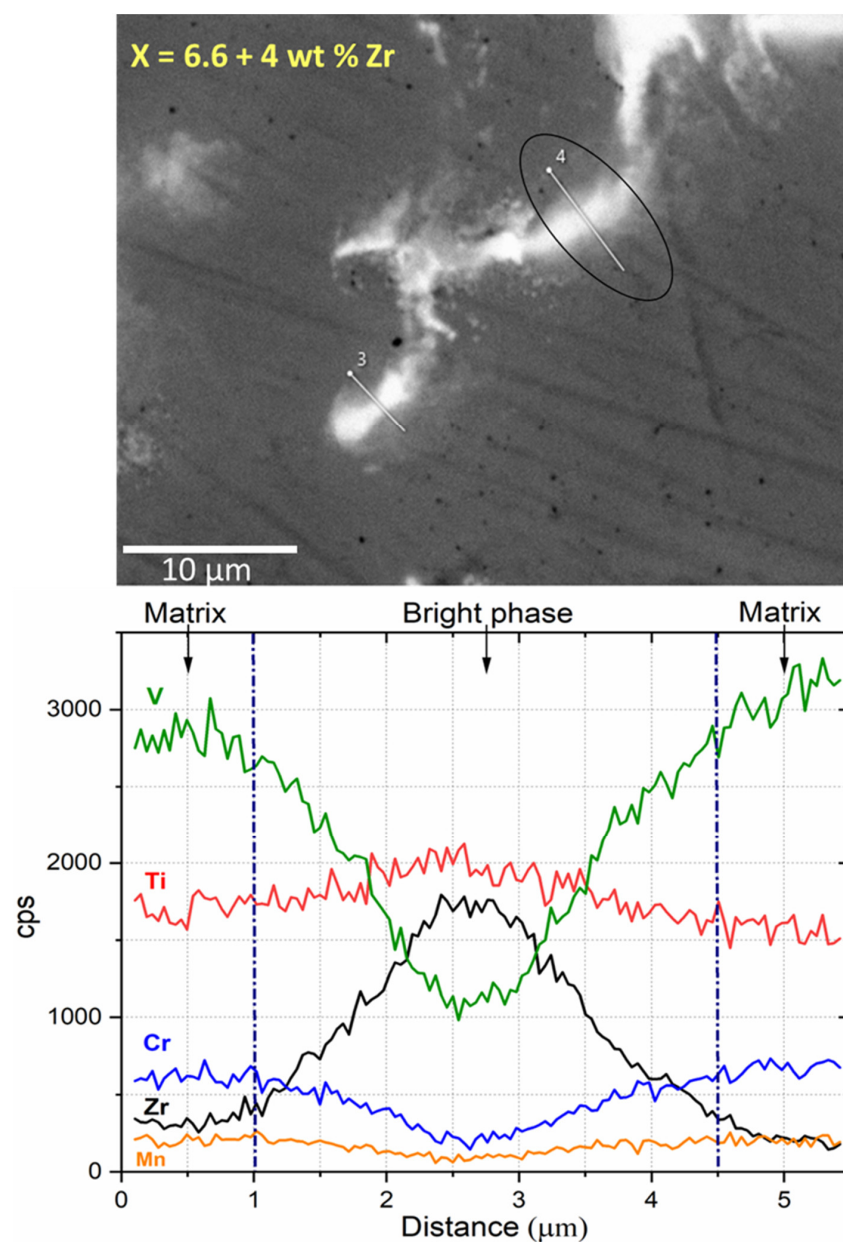

Figure 6. Linear chemical analysis of the as-cast $Ti_{30}V_{60}Mn_{3.3}Cr_{6.6}$ + 4 wt.% Zr alloy. Lines positions are indicated on the SEM micrograph.

As zirconium is mainly present in the bright regions, we wanted to know if another group 4 element would have the same behaviour. Therefore, the effect of adding hafnium instead of zirconium was also investigated. The addition of 8 wt.% Hf was selected in order to keep the same at.% as for the Zr addition. Figure 7 shows the dendritic microstructure of the as-cast $Ti_{30}V_{60}Mn_{3.3}Cr_{6.6}$ + 8 wt.% Hf alloy. Similar to zirconium, the addition of hafnium produced a system consisting of a grey matrix and bright regions.
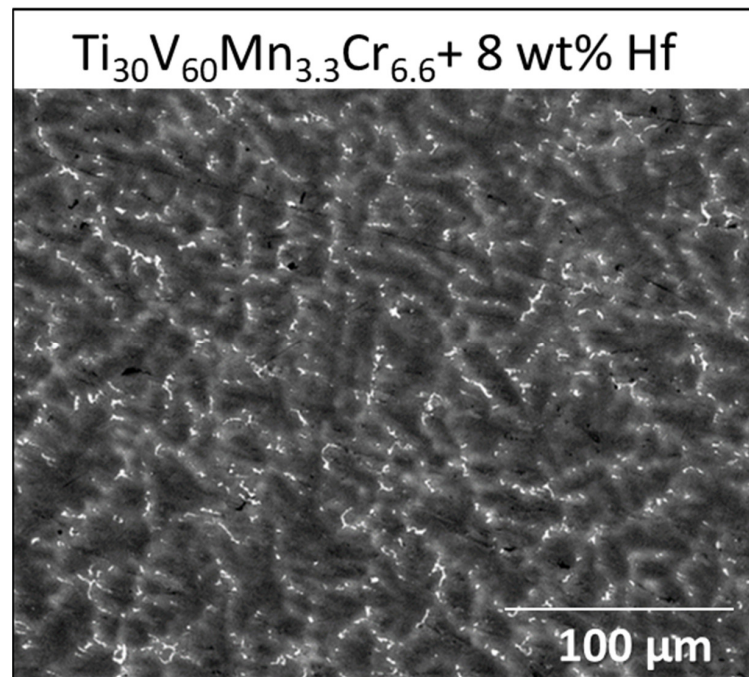

Figure 7. Backscattered electron images of $Ti_{30}V_{60}Mn_{3.3}Cr_{6.6}$ + 8 wt.% Hf alloy.

Figure 8 shows a higher magnification image and element mapping of $Ti_{30}V_{60}Mn_{3.3}Cr_{6.6}$ + 8 wt.% Hf alloy. The chemical composition of the bulk and each specific region was measured by EDX, and the results are presented in Table 2. As for the Zr addition, the matrix composition is close to the nominal value. The bright regions are hafnium rich. Compared with the bright regions of $Ti_{30}V_{60}Mn_{3.3}Cr_{6.6}$ + 4 wt.% Zr, we see that the abundance of titanium, manganese, and chromium is basically the same in the two alloys. The abundance of hafnium is lower than the zirconium abundance while the abundance of vanadium in the bright regions of $Ti_{30}V_{60}Mn_{3.3}Cr_{6.6}$ + 8 wt.% Hf is higher than in the Zr added alloy.
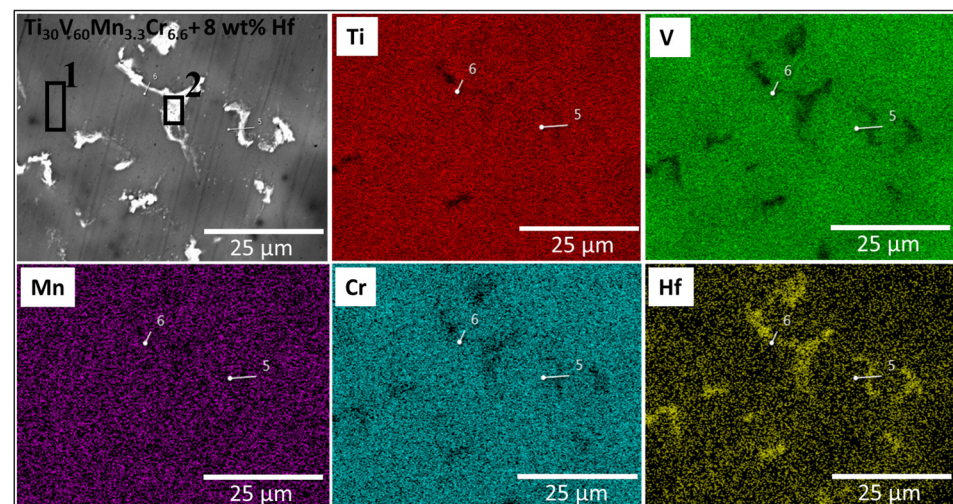

Figure 8. Backscattered electron images of $Ti_{30}V_{60}Mn_{3.3}Cr_{6.6}$ + 8 wt.% Hf alloy with EDX mapping.

Table 2. Chemical composition in at.%, of $Ti_{30}V_{60}Mn_{3.3}Cr_{6.6}$ + 8 wt.% Hf alloys with EDX analysis (uncertainty is ±0.1 for all values).

Sample	Region	Ti (at.%)	V (at.%)	Mn (at.%)	Cr (at.%)	Hf (at.%)
$Ti_{30}V_{60}Mn_{3.3}Cr_{6.6}$ + 8 wt.% Hf	nominal	31	58	3	6	2
	Bulk measured	30.4	57.4	3.4	6.3	2.5
$Ti_{30}V_{60}Mn_{3.3}Cr_{6.6}$ + 8 wt.% Hf	Matrix	29.7	57.4	3.1	5.9	3.9
	Bright Region	41.2	32.6	1.8	3.3	21.1

3.2. Crystal Structure of As-Cast Alloys

The XRD patterns of the alloys as synthesized are shown in Figure 9. For all alloys, only a BCC phase was seen despite the fact that the electron microscopy seems to indicate regions of different chemical compositions. However, as seen in Figure 6, the bright region and the main (matrix) phase smoothly merge into each other. Therefore, considering also the stoichiometry of the bright region, it is possible that it also has a BCC structure with a lattice parameter close to the one of the matrix. However, more proof is needed to support this affirmation. The lack of clear evidence of the existence of a secondary phase leads us to perform the Rietveld refinement assuming a single BCC phase. In the patterns $x = 3.3$ and 10, there may be small peaks at 36°, 38° and 46° but they are too small to be able to clearly assign them to a particular crystal structure. The results of Rietveld refinements are shown in Table 3.

Table 3. Crystal structure parameters of the BCC phase of as-cast alloys $Ti_{30}V_{60}Mn_{(10-x)}Cr_x$ ($x = 0$, 3.3, 6.6, 10) + 4 wt.% Zr. The number in parentheses represents the error on the last digit.

Alloy	Lattice Parameter (Å)	Cell Volume (Å)^3	Crystallite Size (nm)	Microstrain (%)	Average Atomic Radius r (Å)	Ratio r/a
$x = 0$	3.1037(5)	29.90(1)	13.7(4)	0.256(6)	1.3708(4)	0.4416(2)
$x = 3.3$	3.0979(5)	29.71(2)	12.8(2)	0.254(7)	1.3687(4)	0.4418(2)
$x = 6.6$	3.0859(7)	29.52(2)	10.8(2)	0.254(6)	1.3657(4)	0.4425(2)
$x = 10$	3.0962(6)	29.68(2)	11.4(3)	0.252(7)	1.3627(4)	0.4401(2)

Table 3 shows that the lattice parameter of the BCC phase linearly decreased with x value except for $x = 10$ where the lattice parameter increased compared to $x = 6.6$. The reduction of lattice parameters could be explained by the average atomic parameter. Taking the atomic radius of the elements as: Ti (1.46 Å), V (1.32 Å), Mn (1.35 Å), Cr (1.25 Å) and Zr (1.6 Å) [43], the average atomic radius was calculated. The ratio of the lattice parameter to the average atomic radius is reported in Table 3. We see that this ratio is practically constant for $x = 0$, 3.3 and 6.6 but significantly smaller for $x = 10$. Therefore, the change in lattice parameter is partly due to the change in average atomic radius but there are other factors that determine the lattice parameter value. One possibility may be that the $x = 10$ alloy is a ternary alloy while the $x = 3.3$ and 6.6 are quaternary. The crystallite size and microstrains are similar for all compositions. Taking the chemical composition of the bright regions, we calculated the average atomic radius and assuming the same r/a ratio we found that if these regions also have a BCC structure, then the main peak should be at around 38.5 degrees. This seems to correspond to a very small broad peak on the $x = 0$ and $x = 6.6$ patterns. However, this should not be considered reliable proof. More detailed measurements are needed.
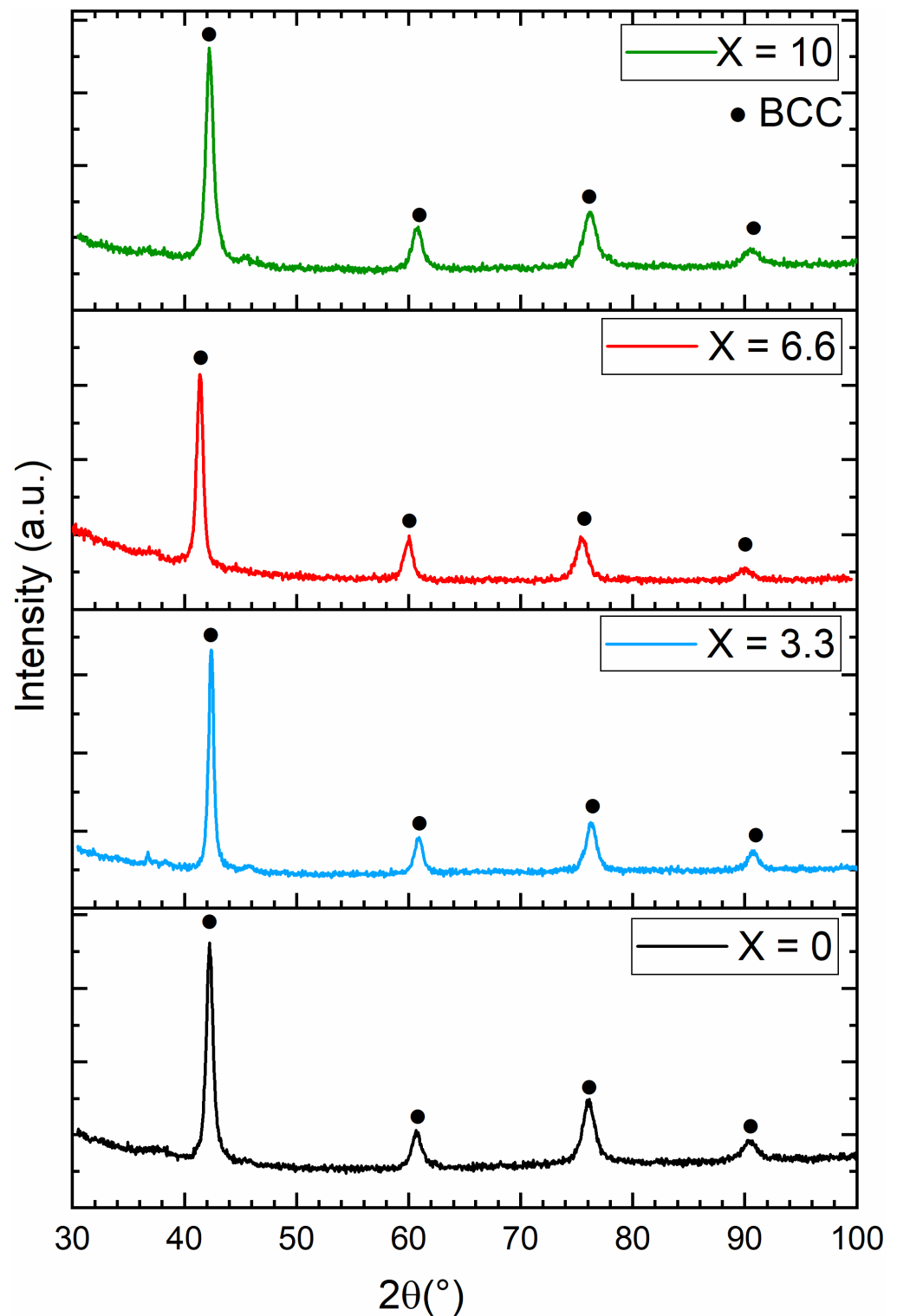
Figure 9. X-ray diffraction patterns of as cast $Ti_{30}V_{60}Mn_{(10-x)}Cr_x$ +4 wt.% Zr alloys with $x = 0$, 3.3, 6.6, and 10.

3.3. First Hydrogenation Properties

The first hydrogenation kinetics of alloys $Ti_{30}V_{60}Mn_{(10-x)}Cr_x$ + 4wt.% Zr (with $x = 0$, 3.3, 6.6 and 10) were measured at 25 °C under a hydrogen pressure of 2 MPa and are shown in Figure 10. All alloys demonstrated a short incubation time and relatively fast kinetics. The alloys without Mn-Cr substitution i.e., $x = 0$ ($Ti_{30}V_{60}Mn_{10}$) and $x = 10$ ($Ti_{30}V_{60}Cr_{10}$) have

a capacity of 3.4 wt.%. This translates to a H/M value of about 1.7. The alloys having both Cr and Mn (x = 3.3 and 6.6) presented the fastest kinetics and highest capacity. The alloy $Ti_{30}V_{60}Mn_{6.6}Cr_{3.3}$ has a capacity of 3.6 wt.% (H/M = 1.8) and the alloy $Ti_{30}V_{60}Mn_{3.3}Cr_{6.6}$ a capacity of 3.8 wt.% (H/M = 1.9).
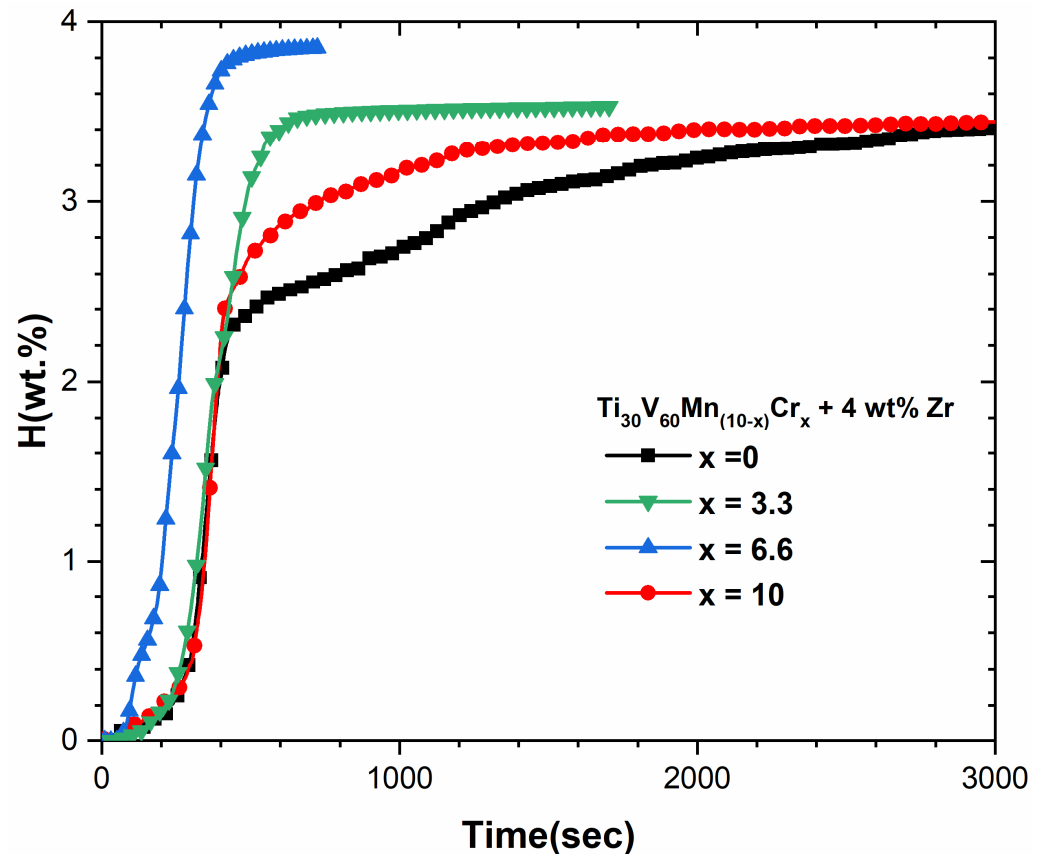

Figure 10. First hydrogenation kinetics of as cast $Ti_{30}V_{60}Mn_{(10-x)}Cr_x$ (x = 0, 3.3, 6.6, and 10) + 4 wt.% Zr alloys under 2 MPa of hydrogen at 25 °C.

The fastest kinetics and the highest capacity were observed for the alloy containing 6.6 at.% Cr. Therefore, the x = 6.6 alloy was selected to study the effect of hafnium addition on the first hydrogenation kinetics. The wt.% of Hf was adjusted in such a way that the same at.% of Hf and Zr was studied. Figure 11 presents the first hydrogenation kinetics of the alloy $Ti_{30}V_{60}Mn_{3.3}Cr_{6.6}$ without additive and with 4 wt.% Zr or 8 wt.% Hf. The Zr addition reaches a maximum capacity of 3.8 wt.% in less than 400 s. For the alloy with 8 wt.% Hf the incubation time is longer, and the maximum capacity is reduced to 3.4 wt.% of hydrogen. Clearly, the variation of hydrogen absorption kinetics is strongly dependent on the nature of the additive.

It is clear from Figure 11 that the alloy x = 6.6 with no zirconium or hafnium does not show activation even after exposing the sample to hydrogen for 17 h. As shown in Figure 1a, the as-cast x = 6.6 without additives has a single-phase microstructure without any bright regions. Therefore, it could be concluded that the presence of Zr or Hf-rich regions has a positive effect on activation. However, it is clear from Figure 11 that, for the same at.% addition, Zr is more effective than Hf in terms of capacity and first hydrogenation kinetics. The reason may be that the main (matrix) and secondary (bright) phases are different. From Tables 1 and 2, we see that the matrix composition of the sample with Zr addition has a much lower abundance of Zr (1.9 at.%) than Hf abundance in the Hf added sample (3.9 at.%). In the same way, the bright phase of the Zr-added sample has a drastically different chemical composition than the secondary phase in the Hf-added sample. Therefore, as the matrix

and secondary phases have different chemistry, the capacity of these phases may be distinct. This may explain the difference in incubation times.
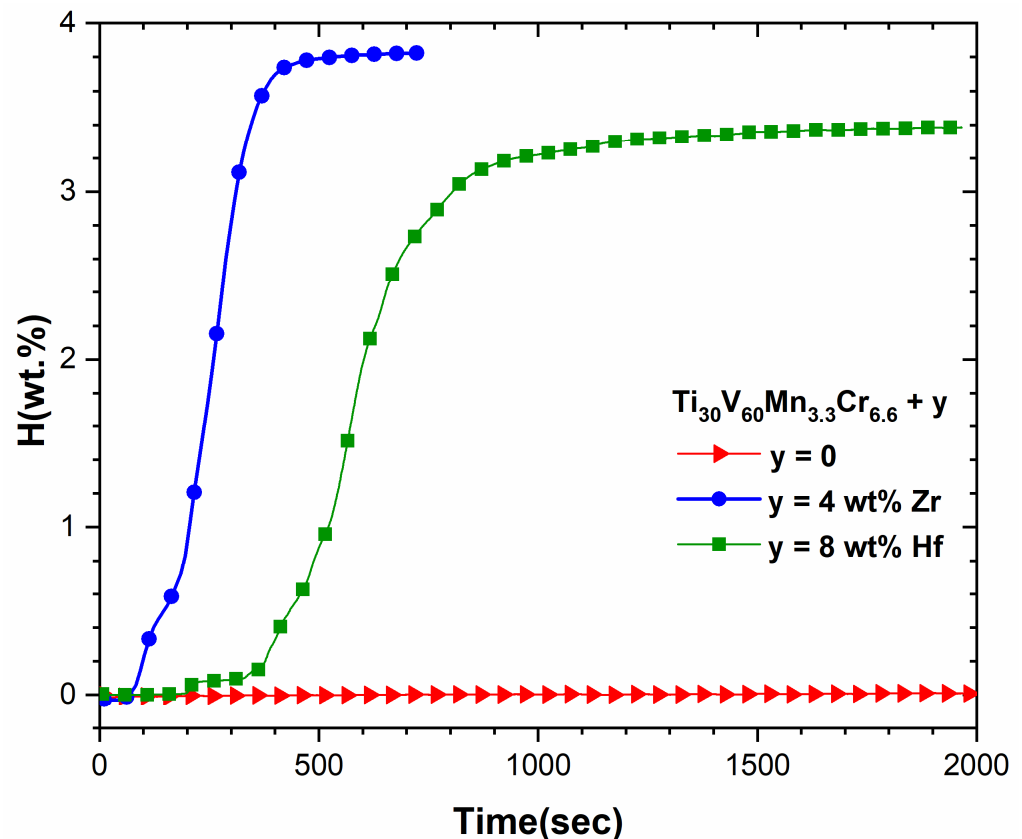

Figure 11. First hydrogenation kinetics at 25 °C under 2 MPa of hydrogen of as cast $Ti_{30}V_{60}Mn_{(3.3}Cr_{6.6}$ alloys with and without additives.

3.4. Crystal Structure of Hydrogenated Alloys

To determine the crystal structure of fully hydrided alloys, the activated $Ti_{30}V_{60}Mn_{(10-x)}Cr_x$ + 4 wt.% Zr alloys were exposed to hydrogen at room temperature under a hydrogen pressure of 2 MPa. The powder diffraction patterns of fully hydrided samples are shown in Figure 12. The refined crystal parameters are listed in Table 4. All the fully hydrogenated alloys crystallize in face-centred cubic (FCC) structures. The unit cells are almost identical, with their volume differing by less than 1.3%. The lattice parameter of the FCC phase is about $\sqrt{2}$ times the BCC lattice parameter which is consistent with full hydrogenation (dihydride) of a BCC phase.

Table 4. Crystal structure parameters of hydrogenated alloys $Ti_{30}V_{60}Mn_{(10-x)}Cr_x$ (x = 0, 3.3, 6.6, 10) + 4 wt.% Zr. The number in parentheses represents the error on the last digit.

Alloy	Lattice Parameter (Å)	Cell Volume (Å)^3	Crystallite Size (nm)	Microstrain (%)
$x = 0$	4.3388(8)	81.68(4)	14.5(6)	0.378(7)
$x = 3.3$	4.3289(5)	81.12(3)	20.4(6)	0.24(4)
$x = 6.6$	4.3219(5)	80.73(3)	20.6(6)	0.268(4)
$x = 10$	4.3276(6)	81.05(3)	15.5(5)	0.312(6)
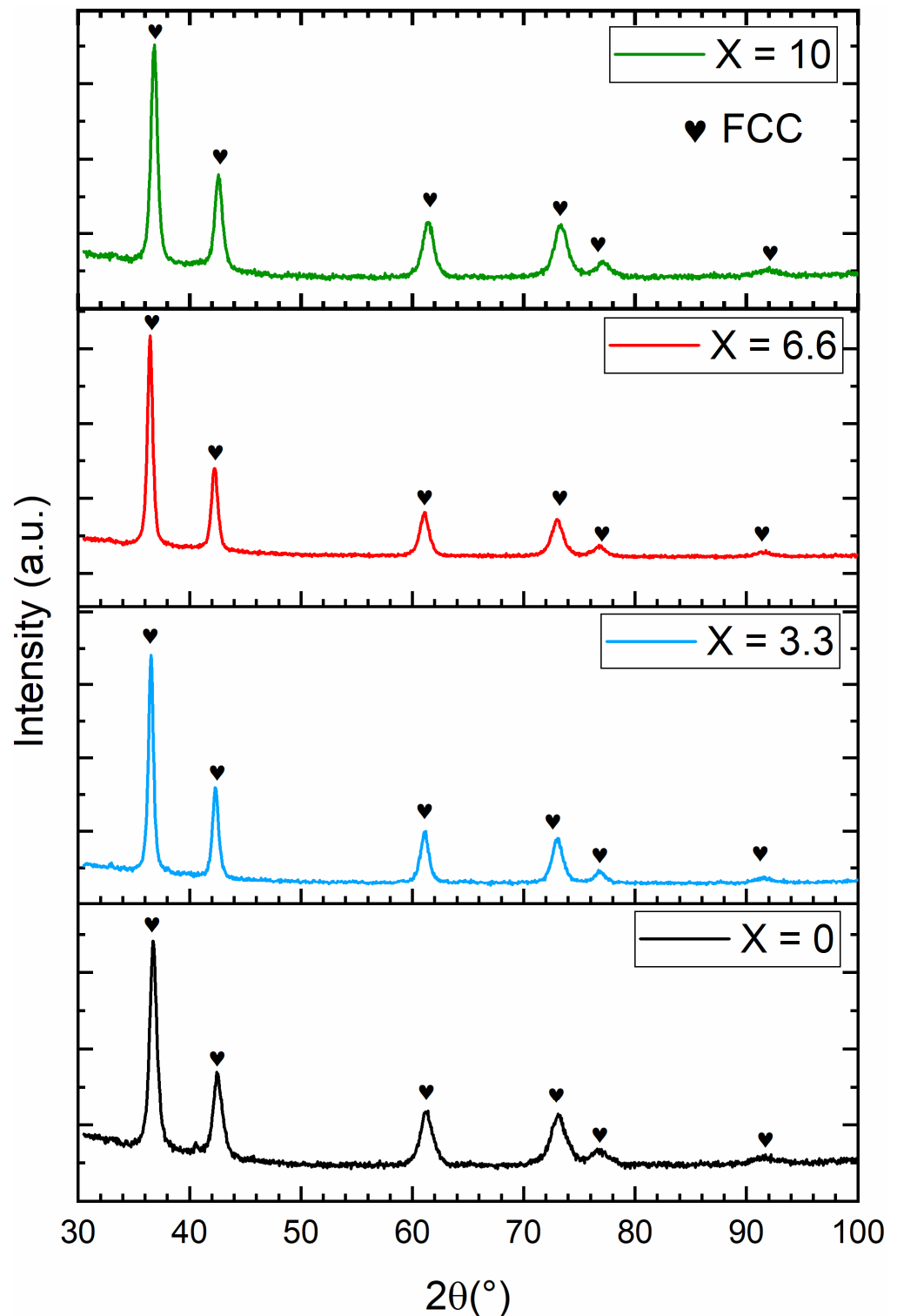
Figure 12. X-ray diffraction patterns of Ti$_{30}$V$_{60}$Mn$_{(10-x)}$Cr$_x$ (x = 0, 3.3, 6.6, 10) + 4 wt.% Zr alloys in the hydrogenated state.

4. Discussion

The microstructure, crystal structure and first hydrogenation of Ti$_{30}$V$_{60}$Mn$_{(10-x)}$Cr$_x$ (x = 0, 3.3, 6.6, 10) with the addition of Zr and Hf were investigated. It was found that Zr and Hf do not mix well in the Ti–V–Cr BCC structure. Instead, they are concentrated in small Zr or Hf-rich regions. The crystal structure of these regions could not be identified but it is spec-

ulated that it may have the BCC structure. The lattice parameter of the BCC phase decreases as the Cr/Mn ratio increases (x increases) and is due to the reduction of the average atomic radius. The first hydrogenation kinetics of $Ti_{30}V_{60}Mn_{(10-x)}Cr_x$ + 4 wt.% Zr is rapid and without any incubation time. Among the four alloys, the $Ti_{30}V_{60}Mn_{3.3}Cr_{6.6}$ + 4 wt.% Zr alloy shows the fastest kinetics and highest hydrogen absorption capacity of 3.8 wt.%. For this composition, adding Hf instead of Zr made the first hydrogenation slower and reduced the capacity to 3.4 wt.%. No activation was observed for the same alloy without additives. This indicates that the presence of a Zr (or Hf) rich region is crucial for fast first hydrogenation.

Author Contributions: Conceptualization, J.H.; validation, C.K. and J.H.; formal analysis, C.K.; investigation, C.K.; writing—original draft preparation, C.K.; writing—review and editing, C.K. and J.H.; supervision, J.H.; project administration, J.H.; funding acquisition, J.H. All authors have read and agreed to the published version of the manuscript.

Data Availability Statement: Data available on request.

Conflicts of Interest: The authors declare no conflict of interest.

References

1. Cho, Y.; Cho, H.; Cho, E.S. Nanointerface Engineering of Metal Hydrides for Advanced Hydrogen Storage. *Chem. Mater.* **2023**, *35*, 366–385. [CrossRef]
2. Kovač, A.; Paranos, M.; Marciuš, D. Hydrogen in energy transition: A review. *Int. J. Hydrogen Energy* **2021**, *46*, 10016–10035. [CrossRef]
3. Zhou, L.; Li, W.; Hu, H.; Zeng, H.; Chen, Q. Ce-doped TiZrCrMn alloys for enhanced hydrogen storage. *Energy Fuels* **2022**, *36*, 3997–4005. [CrossRef]
4. Joubert, J.-M.; Paul-Boncour, V.; Cuevas, F.; Zhang, J.; Latroche, M. LaNi$_5$ related AB$_5$ compounds: Structure, properties and applications. *J. Alloys Compd.* **2021**, *862*, 158163. [CrossRef]
5. Liang, G.; Huot, J.; Schulz, R. Hydrogen storage properties of the mechanically alloyed LaNi$_5$-based materials. *J. Alloys Compd.* **2001**, *320*, 133–139. [CrossRef]
6. Sato, T.; Saitoh, H.; Utsumi, R.; Ito, J.; Nakahira, Y.; Obana, K.; Takagi, S.; Orimo, S.-I. Hydrogen Absorption Reactions of Hydrogen Storage Alloy LaNi$_5$ under High Pressure. *Molecules* **2023**, *28*, 1256. [CrossRef] [PubMed]
7. Lv, P.; Huot, J. Hydrogenation improvement of TiFe by adding ZrMn$_2$. *Energy* **2017**, *138*, 375–382. [CrossRef]
8. Xu, Y.; Deng, Y.; Liu, W.; Zhao, X.; Xu, J.; Yuan, Z. Research progress of hydrogen energy and metal hydrogen storage materials. *Sustain. Energy Technol. Assess.* **2023**, *55*, 102974. [CrossRef]
9. Zhang, Y.; Li, J.; Zhang, T.; Kou, H.; Hu, R.; Xue, X. Microstructural characterization and hydrogenation properties of non-stoichiometric $Zr_{0.9}Ti_xV_2$ alloys. *Int. J. Hydrogen Energy* **2014**, *39*, 19637–19645. [CrossRef]
10. De Rango, P.; Marty, P.; Fruchart, D. Hydrogen storage systems based on magnesium hydride: From laboratory tests to fuel cell integration. *Appl. Phys. A* **2016**, *122*, 126. [CrossRef]
11. Edalati, K.; Akiba, E.; Botta, W.J.; Estrin, Y.; Floriano, R.; Fruchart, D.; Grosdidier, T.; Horita, Z.; Huot, J.; Li, H.-W.; et al. Impact of severe plastic deformation on kinetics and thermodynamics of hydrogen storage in magnesium and its alloys. *J. Mater. Sci. Technol.* **2023**, *146*, 221–239. [CrossRef]
12. Yartys, V.A.; Lototskyy, M.V.; Akiba, E.; Albert, R.; Antonov, V.; Ares, J.-R.; Baricco, M.; Bourgeois, N.; Buckley, C.; von Colbe, J.B.; et al. Magnesium based materials for hydrogen based energy storage: Past, present and future. *Int. J. Hydrogen Energy* **2019**, *44*, 7809–7859. [CrossRef]
13. Zhou, C.; Fang, Z.Z.; Bowman, R.C. Stability of Catalyzed Magnesium Hydride Nanocrystalline during Hydrogen Cycling. Part I: Kinetic Analysis. *J. Phys. Chem. C* **2015**, *119*, 22261–22271. [CrossRef]
14. Ding, N.; Li, Y.; Liang, F.; Liu, B.; Liu, W.; Wang, Q.; Wang, L. Highly Efficient Hydrogen Storage Capacity of 2.5 wt % above 0.1 MPa Using Y and Cr Codoped V-Based Alloys. *ACS Appl. Energy Mater.* **2022**, *5*, 3282–3289. [CrossRef]
15. Mazzolai, G.; Coluzzi, B.; Biscarini, A.; Mazzolai, F.M.; Tuissi, A.; Agresti, F.; Lo Russo, S.; Maddalena, A.; Palade, P.; Principi, G. Hydrogen-storage capacities and H diffusion in bcc TiVCr alloys. *J. Alloys Compd.* **2008**, *466*, 133–139. [CrossRef]
16. Montero, J.; Ek, G.; Laversenne, L.; Nassif, V.; Zepon, G.; Sahlberg, M.; Zlotea, C. Hydrogen storage properties of the refractory Ti–V–Zr–Nb–Ta multi-principal element alloy. *J. Alloys Compd.* **2020**, *835*, 155376. [CrossRef]
17. Okada, M.; Kuriiwa, T.; Tamura, T.; Takamura, H.; Kamegawa, A. Ti–V–Cr b.c.c. alloys with high protium content. *J. Alloys Compd.* **2002**, *330*, 511–516. [CrossRef]

18. Balcerzak, M. Hydrogenation properties of nanocrystalline Ti–V–Mn body-centered-cubic alloys. *Int. J. Hydrogen Energy* **2020**, *45*, 15521–15529. [CrossRef]

19. Song, F.; Yao, J.; Yong, H.; Wang, S.; Xu, X.; Chen, Y.; Zhang, L.; Hu, J. Investigation of ball-milling process on microstructure, thermodynamics and kinetics of Ce–Mg–Ni-based hydrogen storage alloy. *Int. J. Hydrogen Energy* **2023**, *48*, 11274–11286. [CrossRef]

20. Chen, X.; Chen, R.; Ding, X.; Fang, H.; Li, X.; Ding, H.; Su, Y.; Guo, J.; Fu, H. Effect of phase formation on hydrogen storage properties in Ti-V-Mn alloys by zirconium substitution. *Energy* **2019**, *166*, 587–597. [CrossRef]

21. Zhang, Y.; Li, J.; Zhang, T.; Kou, H.; Hu, R.; Xue, X. Hydrogen storage properties of non-stoichiometric $Zr_{0.9}Ti_xV_2$ melt-spun ribbons. *Energy* **2016**, *114*, 1147–1154. [CrossRef]

22. Li, Z.; Yan, Y.; Huang, H.; Liu, B.; Lv, Y.; Zhang, B.; Lv, W.; Yuan, J.; Wu, Y. Effects of the different element substitution on hydrogen storage properties of $Ti_{0.8}Zr_{0.2}Mn_{0.9}Cr_{0.6}V_{0.3}M_{0.2}$ (M = Fe, Ni, Co). *J. Alloys Compd.* **2022**, *908*, 164605. [CrossRef]

23. Nygård, M.M.; Sørby, M.H.; Grimenes, A.A.; Hauback, B.C. The Influence of Fe on the Structure and Hydrogen Sorption Properties of Ti-V-Based Metal Hydrides. *Energies* **2020**, *13*, 2874. [CrossRef]

24. Suwarno, S.; Solberg, J.; Maehlen, J.; Krogh, B.; Yartys, V. Influence of Cr on the hydrogen storage properties of Ti-rich Ti–V–Cr alloys. *Int. J. Hydrogen Energy* **2012**, *37*, 7624–7628. [CrossRef]

25. Tsukahara, M. Hydrogenation properties of vanadium-based alloys with large hydrogen storage capacity. *Mater. Trans.* **2011**, *52*, 68–72. [CrossRef]

26. Young, K.; Ouchi, T.; Nei, J.; Meng, T. Effects of Cr, Zr, V, Mn, Fe, and Co to the hydride properties of Laves phase-related body-centered-cubic solid solution alloys. *J. Power Source* **2015**, *281*, 164–172. [CrossRef]

27. Bibienne, T.; Tousignant, M.; Bobet, J.-L.; Huot, J. Synthesis and hydrogen sorption properties of $TiV_{(2−x)}Mn_x$ BCC alloys. *J. Alloys Compd.* **2015**, *624*, 247–250. [CrossRef]

28. Pickering, L.; Li, J.; Reed, D.; Bevan, A.I.; Book, D. Ti–V–Mn based metal hydrides for hydrogen storage. *J. Alloys Compd.* **2013**, *580*, S233–S237. [CrossRef]

29. Pickering, L.; Reed, D.; Bevan, A.I.; Book, D. Ti–V–Mn based metal hydrides for hydrogen compression applications. *J. Alloys Compd.* **2015**, *645*, S400–S403. [CrossRef]

30. Shashikala, K.; Banerjee, S.; Kumar, A.; Pai, M.; Pillai, C. Improvement of hydrogen storage properties of TiCrV alloy by Zr substitution for Ti. *Int. J. Hydrogen Energy* **2009**, *34*, 6684–6689. [CrossRef]

31. Shibuya, M.; Nakamura, J.; Akiba, E. Hydrogenation properties and microstructure of Ti–Mn-based alloys for hybrid hydrogen storage vessel. *J. Alloys Compd.* **2008**, *466*, 558–562. [CrossRef]

32. Banerjee, S.; Kumar, A.; Ruz, P.; Sengupta, P. Influence of Laves phase on microstructure and hydrogen storage properties of Ti–Cr–V based alloy. *Int. J. Hydrogen Energy* **2016**, *41*, 18130–18140. [CrossRef]

33. Cho, S.-W.; Yoo, J.-H.; Shim, G.; Park, C.-N.; Choi, J. Effects of B addition on the hydrogen absorption–desorption property of $Ti_{0.32}Cr_{0.43}V_{0.25}$ alloy. *Int. J. Hydrogen Energy* **2008**, *33*, 1700–1705. [CrossRef]

34. Feng, Z.; Zhong, H.; Li, D.; Li, X.; Yang, B.; Li, S. Microstructure and hydrogen storage properties of Ti–V–Mn alloy with Zr, Ni, and Zr_7Ni_{10} addition. *J. Mater. Res.* **2022**, *37*, 1591–1601. [CrossRef]

35. Ruz, P.; Banerjee, S.; Halder, R.; Kumar, A.; Sudarsan, V. Thermodynamics, kinetics and microstructural evolution of $Ti_{0.43}Zr_{0.07}Cr_{0.25}V_{0.25}$ alloy upon hydrogenation. *Int. J. Hydrogen Energy* **2017**, *42*, 11482–11492. [CrossRef]

36. Yan, Y.; Chen, Y.; Liang, H.; Wu, C.; Tao, M. Hydrogen storage properties of V_{30}–Ti–Cr–Fe alloys. *J. Alloys Compd.* **2007**, *427*, 110–114. [CrossRef]

37. Hang, Z.; Xiao, X.; Tan, D.; He, Z.; Li, W.; Li, S.; Chen, C.; Chen, L. Microstructure and hydrogen storage properties of $Ti_{10}V_{84−x}Fe_6Zr_x$ (x = 1–8) alloys. *Int. J. Hydrogen Energy* **2010**, *35*, 3080–3086. [CrossRef]

38. Mouri, T.; Iba, H. Hydrogen-absorbing alloys with a large capacity for a new energy carrier. *Mater. Sci. Eng. A* **2002**, *329*, 346–350. [CrossRef]

39. Miraglia, S.; de Rango, P.; Rivoirard, S.; Fruchart, D.; Charbonnier, J.; Skryabina, N. Hydrogen sorption properties of compounds based on BCC $Ti_{1−x}V_{1−y}Cr_{1+x+y}$ alloys. *J. Alloys Compd.* **2012**, *536*, 1–6. [CrossRef]

40. Dixit, V.; Huot, J. Structural, microstructural and hydrogenation characteristics of Ti-V-Cr alloy with Zr-Ni addition. *J. Alloys Compd.* **2019**, *776*, 614–619. [CrossRef]

41. Dixit, V.; Huot, J. Investigation of the microstructure, crystal structure and hydrogenation kinetics of Ti-V-Cr alloy with Zr addition. *J. Alloys Compd.* **2019**, *785*, 1115–1120. [CrossRef]

42. Evans, J.S. Advanced input files & parametric quantitative analysis using topas. *Mater. Sci. Forum.* **2010**, *651*, 1–9. [CrossRef]

43. Miracle, D.B.; Senkov, O.N. A critical review of high entropy alloys and related concepts. *Acta Mater.* **2017**, *122*, 448–511. [CrossRef]